

## Viscoplastic material models for soil: new insight into the soil-support interaction in NATM tunnel excavations

Y. SPIRA, R. LACKNER, CH. PICHLER, H. A. MANG

*Institute for Mechanics of Materials and Structures,  
Vienna University of Technology,  
Karlsplatz 13/202, A-1040 Vienna, Austria*

IN THIS PAPER, the benefits gained from advanced material modeling of soil for the numerical simulation of soil-support interaction in tunneling processes according to the New Austrian Tunneling Method (NATM) are illustrated by means of plane-strain Finite Element (FE) analyses. The studies performed encompass different types of soil (cohesive and granular) and two types of support means (shotcrete lining and jet-grouted soil). As regards the latter, the early-age behavior of the cement-based components is taken into account by means of a coupled chemomechanical approach. The obtained results provide an insight into the benefits gained from the employed support means during NATM tunneling in different geological conditions, serving as the basis in the day-to-day decision process at NATM construction sites. Additionally, effects of the changing geological conditions on the soil-support interaction are illustrated.

**Key words:** tunneling, NATM, soil, shotcrete, jet grouting, chemomechanics, soil-structure interaction.

### 1. Introduction

FOR THE CONSTRUCTION of underground infrastructure, the New Austrian Tunneling Method (NATM) is frequently used. It is characterized by a strong interaction between the deforming ground and the continuously-adopted support means. The latter are installed to provide the safety for the working crew and to minimize the settlements in case of tunneling with low overburden, avoiding damage of the surface buildings and infrastructure.

The proper layout of the support during NATM tunnel excavations is obtained from day-to-day decisions at the construction site, which are based on a closed control cycle consisting of “monitoring – interpretation of results – adaptation of support means”. Whereas the displacement measurements (tunnel convergence and settlements) provide insight into the actual safety at the construction site, numerical schemes are required in order to assess the impact of the adaptation of support means for the next excavation steps. In this paper, the possible contribution of numerical tools to the mentioned day-to-day decision process in NATM tunneling is illustrated for two support means, namely

shotcrete lining and jet-grouted soil, installed in different geological conditions. Also, the impact of changing geological conditions (soil properties and primary conditions) on the soil-support interaction is highlighted.

## 2. Material models

Numerical simulations of the NATM tunneling process need to capture the interaction between the hardening support means (hydrating shotcrete lining and jet-grouted soil) and the viscous soil. Thus, the employed material models must account for the time-dependent behavior of both the soil and support, as will be outlined in the following subsections.

### 2.1. Material models for soil

In order to cover tunneling situations in different geological conditions, two material models for soil were considered in the presented study. These models are employed to describe the mechanical behavior of either cohesive or granular soil:

- For the simulation of the behavior of granular soil, the Mohr–Coulomb criterion is chosen.
- The behavior of cohesive soil is described by the Cam–Clay model, emanating from the critical state theory.

In order to incorporate the creep behavior of soils, both material models were extended towards viscoplasticity. In the following, both material models, their extension to viscoplasticity, and their algorithmic treatment are described.

**2.1.1. Multi-surface plasticity model for granular soil.** During shearing of granular soil, particle movement does not occur exclusively in the direction of the shear force. At low to moderate confining pressures, particles push adjacent grains out of their way or move up and over them. Such pushing or climbing is termed interlocking. It generates an increase of the shear strength of the material and, hence, an increase of the angle of internal friction  $\varphi$ . Figure 1 shows the increase of the shear force resulting from the increase of shear strength by means of a schematic load-displacement curve of a simple-shear test.

After the peak load level has been reached, the load-carrying capacity decreases with increasing deformation. This behavior is associated with the formation of zones of limited thickness where irreversible strains localize. Strain localization causes a change in the local structure of the material. The material is losing its shear resistance (see dashed line in Fig. 1). Finally, when the shear band is fully developed, a residual amount of shear resistance remains. It is characterized by a constant angle of internal friction  $\varphi$ .

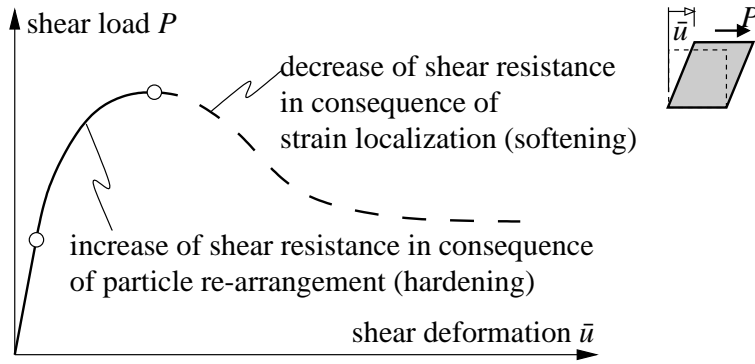


FIG. 1. Schematic plot of the evolution of the shear force obtained from a simple-shear test ( $\bar{u}$ : prescribed displacement).

### *Elastic behavior*

For the Mohr–Coulomb model, an isotropic linear elastic law is employed, reading

$$(2.1) \quad \boldsymbol{\sigma} = \mathbb{C} : \boldsymbol{\varepsilon}, \quad \text{with} \quad \mathbb{C} = \mathbb{C}(E, \nu),$$

with  $\mathbb{C}$  being the (constant) elasticity tensor, depending on the Young's modulus  $E$  and Poisson's ratio  $\nu$ .

### *Yield surfaces*

In the considered material model for granular soil, the change of the friction angle  $\varphi$  is considered in the context of the Mohr–Coulomb yield criterion. The loading function for this criterion is given by

$$(2.2) \quad f_{MC}(\boldsymbol{\sigma}, \kappa_{MC}, k_{MC}) = \frac{1}{2}(\sigma_1 - \sigma_3) + \kappa_{MC} \left[ \frac{1}{2}(\sigma_1 + \sigma_3) - k_{MC} \right],$$

where  $\sigma_1$  and  $\sigma_3$  represent the largest and the smallest principal stress.  $\kappa_{MC}$  and  $k_{MC}$  are material parameters. They are defined by

$$(2.3) \quad \kappa_{MC} = \sin \varphi \quad \text{and} \quad k_{MC} = \frac{c}{\tan \varphi},$$

where  $c$  denotes the cohesion. For description of the material response under tensile loading, the tension-cut-off criterion is employed. It is characterized by the following loading function:

$$(2.4) \quad f_{TC}(\boldsymbol{\sigma}) = I_1 - f_t.$$

$I_1$  denotes the first invariant of the stress tensor;  $f_t$  represents the uniaxial tensile strength of the material which, in general, is negligible.

*Plastic flow rule*

Granular soils exhibit volume dilation when subjected to shear deformations. Use of an associative flow rule for the described Mohr–Coulomb criterion (see Eq. (2.2)) would result in an overestimation of this dilation. Consequently, a non-associative flow rule is adopted. The plastic potential  $g_{MC}$  is obtained from modification of the Mohr–Coulomb criterion (Eq. (2.2)) with respect to its volumetric part, reading

$$(2.5) \quad g_{MC} = \frac{1}{2}(\sigma_1 - \sigma_3) + \bar{\kappa}_{MC} \frac{1}{2}(\sigma_1 + \sigma_3) .$$

$\bar{\kappa}_{MC}$  is related to the angle of dilatancy  $\psi$  in the same way as  $\kappa_{MC}$  to  $\varphi$  in Eq. (2.3) [4], reading

$$(2.6) \quad \bar{\kappa}_{MC} = \sin \psi .$$

For the tension-cut-off, an associative flow rule is used, finally giving the evolution equation for the plastic strain tensor as

$$(2.7) \quad \dot{\boldsymbol{\varepsilon}}^p = \dot{\gamma}_{MC} \frac{\partial g_{MC}}{\partial \boldsymbol{\sigma}} + \dot{\gamma}_{TC} \frac{\partial f_{TC}}{\partial \boldsymbol{\sigma}} ,$$

where  $\gamma_{MC}$  and  $\gamma_{TC}$  are consistency parameters.

*Hardening rule*

Whereas ideally-plastic behavior is assumed for the tension-cut-off, isotropic hardening is considered in the context of the Mohr–Coulomb criterion. Hereby, two basic modes of isotropic hardening can be distinguished [35]: cohesion and friction hardening (Fig. 2). For modeling of cohesionless materials such as granular soils, friction hardening is appropriate [20]. Accordingly,  $k_{MC}$  is set equal to

$$(2.8) \quad k_{MC} = \frac{c}{\tan \varphi_p} = \text{constant} ,$$

where  $\varphi_p$  denotes the peak value of the friction angle  $\varphi$ . Friction hardening is controlled by the value of  $\kappa_{MC}$  in Eq. (2.2). A quadratic increase of  $\kappa_{MC}$  from  $\kappa_{MC,i} = \sin \varphi_i$  to  $\kappa_{MC,p} = \sin \varphi_p$  is considered:

$$(2.9) \quad \kappa_{MC} = \kappa_{MC,i} + (\kappa_{MC,p} - \kappa_{MC,i}) \left[ 1 - \frac{(\chi_{MC} - \bar{\chi}_{MC})^2}{\bar{\chi}_{MC}^2} \right]$$

for  $\chi_{MC} < \bar{\chi}_{MC}$ , where  $\bar{\chi}_{MC}$  is a calibration parameter. For  $\chi_{MC} \geq \bar{\chi}_{MC}$ ,  $\kappa_{MC} = \kappa_{MC,p} = \text{constant}$ . The evolution of  $\kappa_{MC}$  is controlled by means of the

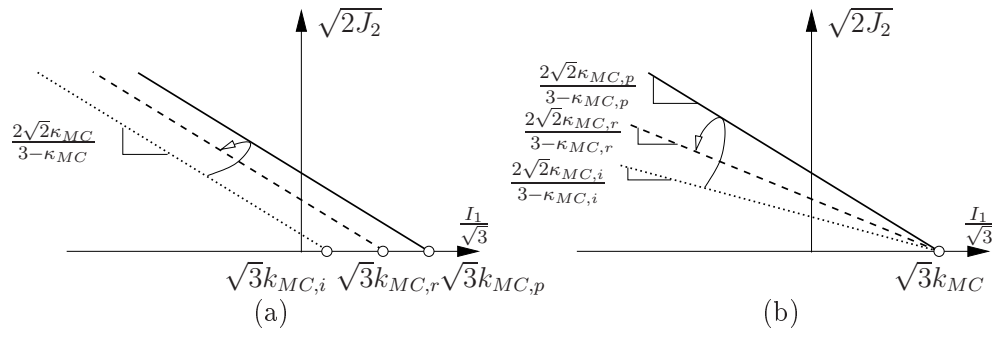


FIG. 2. Illustration of hardening in the framework of the Mohr–Coulomb criterion (compressive meridian): (a) cohesion and (b) friction hardening (subscripts  $i$  and  $p$  refer to the initial and the peak value, respectively).

strain-like internal variable  $\chi_{MC}$ . Since friction hardening is connected with deviatoric deformations,  $\chi_{MC}$  is related to the deviatoric part of the plastic strain tensor,  $\mathbf{e}^p$  [35, 23, 29]:

$$(2.10) \quad \dot{\chi}_{MC} = \sqrt{\frac{2}{3}} \dot{\mathbf{e}}^{p,T} : \dot{\mathbf{e}}^p = \sqrt{\frac{2}{3}} \|\dot{\mathbf{e}}^p\| .$$

Consideration of  $\dot{\mathbf{e}}^p = \dot{\gamma}_{MC} \partial g_{MC} / \partial \mathbf{s}$  in Eq. (2.10), where  $\mathbf{s}$  denotes the deviatoric stress tensor, gives

$$(2.11) \quad \dot{\chi}_{MC} = \dot{\gamma}_{MC} \sqrt{\frac{2}{3}} \left\| \frac{\partial g_{MC}}{\partial \mathbf{s}} \right\| .$$

#### Angle of dilatancy $\psi$

The change in dilatancy of granular soils during shear loading is taken into account by a variable angle of dilatancy  $\psi$  [35]. Under medium compressive loading, the angle of dilatancy  $\psi$  is assumed to increase during shear deformation from an initial value  $\psi_i$  to a peak value  $\psi_p$ . The respective values of  $\bar{\kappa}_{MC}$  are obtained as

$$(2.12) \quad \bar{\kappa}_{MC,i} = \sin \psi_i \quad \text{and} \quad \bar{\kappa}_{MC,p} = \sin \psi_p .$$

The increase of  $\bar{\kappa}_{MC}$  is considered in a similar manner as the increase of  $\kappa_{MC}$  according to Eq. (2.9) [34], reading

$$(2.13) \quad \bar{\kappa}_{MC} = \bar{\kappa}_{MC,i} + (\bar{\kappa}_{MC,p} - \bar{\kappa}_{MC,i}) \left[ 1 - \frac{(\chi_{MC} - \bar{\chi}_{MC})^2}{\bar{\chi}_{MC}^2} \right]$$

for  $\chi_{MC} < \bar{\chi}_{MC}$ . For  $\chi_{MC} \geq \bar{\chi}_{MC}$ ,  $\bar{\kappa}_{MC} = \bar{\kappa}_{MC,p} = \text{constant}$ .

*Kuhn–Tucker and consistency conditions*

Finally, the Kuhn–Tucker loading/unloading conditions

$$(2.14) \quad f_k \leq 0, \quad \dot{\gamma}_k \geq 0, \quad \dot{\gamma}_k f_k = 0,$$

as well as the consistency condition

$$(2.15) \quad \dot{\gamma}_k \dot{f}_k = 0$$

are employed, with  $k \in \{MC, TC\}$ .

*Algorithmic formulation – integration of evolution equations*

For the integration of the evolution equations [Eq. (2.7) and Eq. (2.11)], an implicit integration scheme is applied. For the  $(n + 1)$ -st load increment, with  $t_n \leq t \leq t_{n+1}$ , time integration yields the plastic strain tensor and the internal variable at  $t_{n+1}$ <sup>1)</sup>:

$$(2.16) \quad \boldsymbol{\varepsilon}_{n+1}^p = \boldsymbol{\varepsilon}_n^p + \Delta\gamma_{MC} \frac{\partial g_{MC}}{\partial \boldsymbol{\sigma}} + \Delta\gamma_{TC} \frac{\partial f_{TC}}{\partial \boldsymbol{\sigma}},$$

$$(2.17) \quad \chi_{MC,n+1} = \chi_{MC,n} + \Delta\gamma_{MC} \sqrt{\frac{2}{3}} \left\| \frac{\partial g_{MC}}{\partial \mathbf{s}} \right\|.$$

Equations (2.16) and (2.17) represent a set of nonlinear equations for the unknowns  $\boldsymbol{\varepsilon}_{n+1}^p$ ,  $\chi_{MC,n+1}$ ,  $\Delta\gamma_{MC}$ , and  $\Delta\gamma_{TC}$ , collected in the vector  $\mathbf{x}$ , with  $\mathbf{x} = [\boldsymbol{\varepsilon}_{n+1}^p, \chi_{MC,n+1}, \Delta\gamma_{MC}, \Delta\gamma_{TC}]^T$ . The respective residual form of the Eqs. (2.16) and (2.17) reads

$$(2.18) \quad \mathbf{R}(\mathbf{x}) = \left\{ \begin{array}{c} -\boldsymbol{\varepsilon}_{n+1}^p + \boldsymbol{\varepsilon}_n^p + \Delta\gamma_{MC} \frac{\partial g_{MC}}{\partial \boldsymbol{\sigma}} + \Delta\gamma_{TC} \frac{\partial f_{TC}}{\partial \boldsymbol{\sigma}} \\ -\chi_{MC,n+1} + \chi_{MC,n} + \Delta\gamma_{MC} \sqrt{\frac{2}{3}} \left\| \frac{\partial g_{MC}}{\partial \mathbf{s}} \right\| \\ f_{MC} \\ f_{TC} \end{array} \right\} = \mathbf{0},$$

where the case of two active yield surfaces is considered. Accordingly, the constraint conditions  $f_{MC} = 0$  and  $f_{TC} = 0$  appear in the residual  $\mathbf{R}$ . For determination of the vector of unknowns,  $\mathbf{x}$ , from Eq. (2.18), the Newton scheme is employed, reading

$$(2.19) \quad \mathbf{R} + \frac{d\mathbf{R}}{d\mathbf{x}} \Delta\mathbf{x} = \mathbf{0}.$$

<sup>1)</sup>In Eqs. (2.16) and (2.17), both the Mohr–Coulomb criterion and the tension-cut-off are assumed to be active and, thus, contribute to the evolution of the plastic strain tensor. In the following, this (most general) case will be considered. The case of only one yield criterion being active is easily obtained by eliminating the respective entries in the subsequent equations.

During the Newton iteration, history variables corresponding to the previous load increment and the prescribed strains at  $t_{n+1}$  remain constant. Hence, the differentials of these quantities are zero, i.e.

$$(2.20) \quad d\boldsymbol{\varepsilon}_n^p = \mathbf{0}, \quad d\chi_{MC,n} = 0, \quad \text{and} \quad d\boldsymbol{\varepsilon}_{n+1} = \mathbf{0}.$$

Accounting for  $d\boldsymbol{\sigma}_{n+1} = \mathbf{C}(d\boldsymbol{\varepsilon}_{n+1} - d\boldsymbol{\varepsilon}_{n+1}^p) = \mathbf{C}(-d\boldsymbol{\varepsilon}_{n+1}^p)$ , with  $\mathbf{C}$  as the elasticity matrix, and introducing  $\bar{D} = -d\bar{\kappa}_{MC}/d\chi_{MC}$  and  $D = -d\kappa_{MC}/d\chi_{MC}$ , the matrix  $d\mathbf{R}/d\mathbf{x}$  in Eq. (2.19) becomes

$$(2.21) \quad \frac{d\mathbf{R}}{d\mathbf{x}} = \left[ \begin{array}{c|cc} \mathbf{A}^{-1} & \nabla g_{MC} & \nabla f_{TC} \\ \hline \nabla f_{MC}^T & 0 & 0 \\ \nabla f_{TC}^T & 0 & 0 \end{array} \right] \left[ \begin{array}{cc|cc} -\mathbf{C} & \mathbf{0} & \mathbf{0} & \mathbf{0} \\ \mathbf{0}^T & -D & 0 & 0 \\ \mathbf{0}^T & 0 & 1 & 0 \\ \mathbf{0}^T & 0 & 0 & 1 \end{array} \right]$$

with

$$(2.22) \quad \mathbf{A}^{-1} = \left[ \begin{array}{cc} \mathbf{C}^{-1} & \Delta\gamma_{MC} \frac{\partial^2 g_{MC}}{\partial \boldsymbol{\sigma} \partial \bar{\kappa}_{MC}} \bar{D} D^{-1} \\ \mathbf{0}^T & D^{-1} + \Delta\gamma_{MC} \sqrt{\frac{2}{3}} \left\| \frac{\partial g_{MC}}{\partial \mathbf{s}} \right\|^{-1} \frac{\partial^2 g_{MC}}{\partial \mathbf{s} \partial \bar{\kappa}_{MC}} \bar{D} D^{-1} \end{array} \right],$$

and

$$(2.23) \quad \nabla g_{MC} = \left\{ \begin{array}{c} \frac{\partial g_{MC}}{\partial \boldsymbol{\sigma}} \\ \sqrt{\frac{2}{3}} \left\| \frac{\partial g_{MC}}{\partial \mathbf{s}} \right\| \end{array} \right\}, \quad \nabla f_{MC} = \left\{ \begin{array}{c} \frac{\partial f_{MC}}{\partial \boldsymbol{\sigma}} \\ \frac{\partial f_{MC}}{\partial \kappa_{MC}} \end{array} \right\}, \quad \nabla f_{TC} = \left\{ \begin{array}{c} \frac{\partial f_{TC}}{\partial \boldsymbol{\sigma}} \\ 0 \end{array} \right\}.$$

After time integration, i.e., after convergence of the Newton iteration, the stresses are given by  $\boldsymbol{\sigma}_{n+1} = \mathbf{C}(\boldsymbol{\varepsilon}_{n+1} - \boldsymbol{\varepsilon}_{n+1}^p)$ . For the evaluation of the consistent tangent  $\mathbf{C}_T$ , the time integration algorithm is linearized in closed form [27]. For this purpose, the differential form of the discrete (algorithmic) flow rules and the yield criteria are required:

$$(2.24) \quad d\mathbf{R}(\mathbf{x}_{n+1}) = \mathbf{0}.$$

Use of the differential form of the constitutive law,  $d\boldsymbol{\sigma}_{n+1} = \mathbf{C}(d\boldsymbol{\varepsilon}_{n+1} - d\boldsymbol{\varepsilon}_{n+1}^p)$ , leads to the following system of equations with the unknowns  $d\boldsymbol{\sigma}_{n+1}$ ,  $d\kappa_{MC,n+1}$ ,  $d\Delta\gamma_{MC}$  and  $d\Delta\gamma_{TC}$ :

$$(2.25) \quad d\mathbf{R} = \left[ \begin{array}{c|cc} \mathbf{A}^{-1} & \nabla g_{MC} & \nabla f_{TC} \\ \hline \nabla f_{MC}^T & 0 & 0 \\ \nabla f_{TC}^T & 0 & 0 \end{array} \right] \left\{ \begin{array}{c} d\boldsymbol{\sigma}_{n+1} \\ d\kappa_{MC,n+1} \\ d\Delta\gamma_{MC} \\ d\Delta\gamma_{TC} \end{array} \right\} - \left\{ \begin{array}{c} d\boldsymbol{\varepsilon}_{n+1} \\ 0 \\ 0 \\ 0 \end{array} \right\} = \mathbf{0}.$$

Solving Eq. (2.25) for  $[d\boldsymbol{\sigma}_{n+1}, d\kappa_{MC,n+1}]^T$  gives

$$(2.26) \quad \begin{Bmatrix} d\boldsymbol{\sigma}_{n+1} \\ d\kappa_{MC,n+1} \end{Bmatrix} = \begin{bmatrix} \mathbf{A} & -\mathbf{g}_{11}^{\text{inv}} \mathbf{A} \nabla g_{MC} \nabla f_{MC}^T \mathbf{A} \\ & -\mathbf{g}_{12}^{\text{inv}} \mathbf{A} \nabla g_{MC} \nabla f_{TC}^T \mathbf{A} \\ & -\mathbf{g}_{21}^{\text{inv}} \mathbf{A} \nabla f_{TC} \nabla f_{MC}^T \mathbf{A} \\ & -\mathbf{g}_{22}^{\text{inv}} \mathbf{A} \nabla f_{TC} \nabla f_{TC}^T \mathbf{A} \end{bmatrix} \begin{Bmatrix} d\boldsymbol{\varepsilon}_{n+1} \\ 0 \end{Bmatrix},$$

where  $\mathbf{g}^{\text{inv}} = \mathbf{g}^{-1}$  and

$$(2.27) \quad \mathbf{g} = \begin{bmatrix} \nabla f_{MC}^T \mathbf{A} \nabla g_{MC} & \nabla f_{MC}^T \mathbf{A} \nabla f_{TC} \\ \nabla f_{TC}^T \mathbf{A} \nabla g_{MC} & \nabla f_{TC}^T \mathbf{A} \nabla f_{TC} \end{bmatrix}.$$

The consistent tangent  $\mathbf{C}_T$  is obtained by extracting  $d\boldsymbol{\sigma}_{n+1} = \mathbf{C}_{T,n+1} d\boldsymbol{\varepsilon}_{n+1}$  from Eq. (2.27). It is noteworthy that because of the non-associative flow rule considered for the Mohr–Coulomb criterion  $\mathbf{C}_T$  is non-symmetric, resulting in a non-symmetric tangent matrix for finite element (FE) analysis. In case of an associative flow rule, characterized by  $g_{MC} = f_{MC}$ ,  $\mathbf{C}_T$  becomes symmetric.

#### *Extension to viscoplasticity*

The described multi-surface plasticity model is extended to viscoplasticity by means of the law of DUBAUT–LIONS [8] which is well-suited for application to multi-surface plasticity models [28]. Hereby, the stresses  $\boldsymbol{\sigma}$  are given as

$$(2.28) \quad \boldsymbol{\sigma} = \mathbb{C} : (\boldsymbol{\varepsilon} - \boldsymbol{\varepsilon}^{\text{vp}}),$$

where  $\boldsymbol{\varepsilon}^{\text{vp}}$  denotes the viscoplastic strain tensor. The evolution laws for the viscoplastic strains and for the hardening parameter read

$$(2.29) \quad \dot{\boldsymbol{\varepsilon}}^{\text{vp}} = \frac{1}{\tau} \mathbb{C}^{-1} : (\boldsymbol{\sigma} - \boldsymbol{\sigma}^\infty) \quad \text{and} \quad \dot{\kappa}_{MC} = -\frac{1}{\tau} (\kappa_{MC} - \kappa_{MC}^\infty),$$

where  $\tau$  denotes the relaxation time and  $\boldsymbol{\sigma}^\infty$  and  $\kappa_{MC}^\infty$  correspond to the solution for infinitely slow loading, coinciding with the stress state and hardening parameter of rate-independent plasticity (solution of Eq. (2.18)).

**2.1.2. Single-surface plasticity model for cohesive soil.** A good description of the behavior of cohesive soils, i. e., clays, yields the so-called critical state theory [25]. This theory is based on the observation that under continued shearing cohesive

material seems to reach a state, where volumetric strains become constant and the stress state does not change any more [25]. This specific state, where the soil behaves like a purely frictional material, is called a *critical state*, and is adequately described by a Cam–Clay type plasticity model as outlined in the following.

### *Elastic behavior*

According to experimental observations, the bulk modulus  $K$  is found to depend linearly on the hydrostatic pressure. Furthermore, experimental observations by HOULSBY [18] revealed, that the shear modulus  $G$  varies also with the hydrostatic pressure. Based thereon, HOULSBY proposed the function of the stored energy [18], which takes coupling between the volumetric and deviatoric response into account:

$$(2.30) \quad \mathcal{W}(\boldsymbol{\varepsilon}^e) = t \frac{\kappa}{v_0} \exp\left(\frac{-v_0}{\kappa} \bar{I}_1^e\right) \left(1 + \tilde{\alpha} \frac{v_0}{\kappa} 2\bar{J}_2^e\right).$$

In Eq. (2.30),  $t$  denotes the hydrostatic tensile strength, generally being very small.  $\kappa$  stands for the slope of the unloading-reloading curve in a semi-logarithmic hydrostatic pressure – specific volume diagram; and  $v_0$  is the value of the initial specific volume  $v$  defined as  $v = V_{\text{actual}}/V_{\text{solid particles}}$  (see, e.g., [37]).  $\bar{I}_1^e$  and  $\bar{J}_2^e$  are the first and second invariant of the strain tensor and deviatoric strain tensor, respectively. The parameter  $\tilde{\alpha}$  is a measure for the amount of the coupling between the volumetric and deviatoric response. For predominantly deviatoric strains and small volumetric strains, however, the stored-energy function in Eq. (2.30) leads to unreasonable stress-paths in the elastic range.

As a remedy, a modified form of the stored energy function  $\mathcal{W}(\boldsymbol{\varepsilon}^e)$  is used here, reading

$$(2.31) \quad \mathcal{W}(\boldsymbol{\varepsilon}^e) = t \frac{\kappa}{v_0} \left(1 + \tilde{\alpha} \frac{v_0}{\kappa} 2\bar{J}_2^e\right) \left[\exp\left(\frac{-v_0}{\kappa} \bar{I}_1^e\right) + \exp\left(\frac{v_0}{\kappa} \bar{I}_1^e\right)\right] - 2t \frac{\kappa}{v_0}.$$

This function is convex in the strain space and the shift term  $2t\kappa/v_0$  guarantees zero energy in the undeformed configuration. The elastic law and the elastic tangent are obtained from Eq. (2.31) as

$$(2.32) \quad \boldsymbol{\sigma} = \frac{\partial \mathcal{W}}{\partial \boldsymbol{\varepsilon}^e} = t \left(1 + \tilde{\alpha} \frac{v_0}{\kappa} 2\bar{J}_2^e\right) \left[-\exp\left(\frac{-v_0}{\kappa} \bar{I}_1^e\right) + \exp\left(\frac{v_0}{\kappa} \bar{I}_1^e\right)\right] \mathbf{1} \\ + 2\tilde{\alpha} t \left[\exp\left(\frac{-v_0}{\kappa} \bar{I}_1^e\right) + \exp\left(\frac{v_0}{\kappa} \bar{I}_1^e\right)\right] \boldsymbol{\varepsilon}_{\text{dev}}^e,$$

$$\begin{aligned}
(2.33) \quad \mathbb{C} = & \frac{\partial^2 \mathcal{W}}{\partial \boldsymbol{\varepsilon}^e \otimes \partial \boldsymbol{\varepsilon}^e} t \frac{v_0}{\kappa} \left( 1 + \tilde{\alpha} \frac{v_0}{\kappa} 2\bar{J}_2^e \right) \left[ \exp \left( \frac{-v_0}{\kappa} \bar{I}_1^e \right) + \exp \left( \frac{v_0}{\kappa} \bar{I}_1^e \right) \right] \mathbf{1} \otimes \mathbf{1} \\
& + 2\tilde{\alpha} t \left[ \exp \left( \frac{-v_0}{\kappa} \bar{I}_1^e \right) + \exp \left( \frac{v_0}{\kappa} \bar{I}_1^e \right) \right] \mathbb{I}_{\text{dev}} \\
& - 2\tilde{\alpha} t \frac{v_0}{\kappa} \left[ -\exp \left( \frac{-v_0}{\kappa} \bar{I}_1^e \right) + \exp \left( \frac{v_0}{\kappa} \bar{I}_1^e \right) \right] (\boldsymbol{\varepsilon}_{\text{dev}}^e \otimes \mathbf{1} + \mathbf{1} \otimes \boldsymbol{\varepsilon}_{\text{dev}}^e).
\end{aligned}$$

### *Yield surfaces*

For the Modified Cam–Clay model, the elastic domain is bounded by a single yield surface in the  $p - \sqrt{3J_2}$  stress space (see Fig. 3), with  $M$  denoting the slope of the critical state line and  $q_{CC}$  standing for the actual size of the ellipse. This form of the yield surface agrees well with experiments on clay. It is described by the function

$$(2.34) \quad f_{CC}(\boldsymbol{\sigma}, q_{CC}) = \sqrt{3J_2 + M^2 \left( p - t + \frac{q_{CC}}{2} \right)^2} - M \frac{q_{CC}}{2}.$$

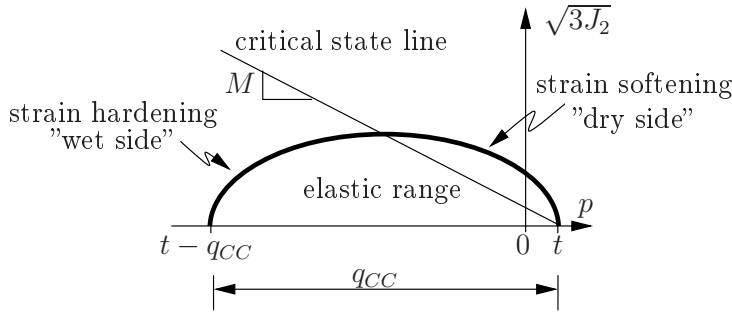


FIG. 3. Yield surface of the Cam–Clay model in the stress space.

### *Plastic flow rule*

Cohesive soil can experience volume dilation as well as volume compaction under shear deformation. The type of volumetric deformation occurring depends on the actual density of the material, represented by the size of the ellipsoidal yield surface, and on the stress path in the  $p - \sqrt{3J_2}$  stress space. Experiments made on the undisturbed Winnipeg clay (see [37]) indicate normality of plastic strain increments with respect to the current yield surface. Therefore, the

evolution of the plastic strains is assumed to be associative, reading as

$$(2.35) \quad \dot{\boldsymbol{\epsilon}}^p = \dot{\gamma}_{CC} \frac{\partial f_{CC}}{\partial \boldsymbol{\sigma}}.$$

#### Hardening/softening rule

Depending on the loading state, strain hardening or strain softening is captured by the model. On the “dry” side of the critical state line (see Fig. 3), loading of clays exhibits a softening behavior connected with a volume increase. On the “wet” side of this line, hardening connected with compaction occurs. The total volumetric strains are decomposed into an elastic and a plastic part. Using the information contained in Fig. 4, this results in the following relation:

$$(2.36) \quad \bar{I}_1 = \frac{(v - v_0)}{v_0} = \bar{I}_1^e + \bar{I}_1^p = \frac{(v - v_\kappa)}{v_0} + \frac{(v_\kappa - v_0)}{v_0},$$

with  $v$ ,  $v_\kappa$ , and  $v_0$  denoting the actual specific volume, the specific volume corresponding to the hydrostatic pressure  $-(p_0 - t)$ , and the initial specific volume, respectively. Inserting the expression for  $(v_\kappa - v_0)$  given in Fig. 4 into  $\bar{I}_1^p = (v_\kappa - v_0)/v_0$  (Eq. (2.36)), the nonlinear hardening law

$$(2.37) \quad q_{CC} = (q_0 - t) \exp\left(\frac{-v_0}{\lambda - \kappa} \bar{I}_1^p\right) + t$$

is obtained, with  $q_0$  as the initial preconsolidation pressure and  $\lambda$  as the slope of the normal compression line. According to Eq. (2.37), the evolution of the yield surface depends exclusively on volumetric plastic strain.

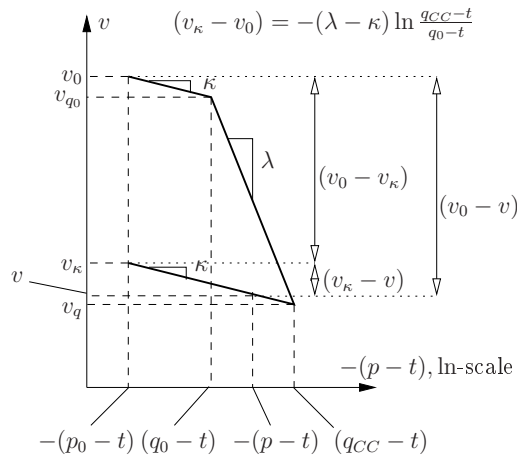


FIG. 4. Linear relation between  $v$  and  $-(p - t)$ , ln-scale.

*Kuhn–Tucker and consistency conditions*

As in the previous material model, the Kuhn–Tucker loading/unloading conditions and the consistency condition are included in the model.

*Algorithmic formulation – integration of evolution equations*

Similarly to the previously described multi-surface model, an implicit integration scheme is employed for the time integration of the evolution equations [27], yielding the residual expression as

$$(2.38) \quad \mathbf{R}(\mathbf{x}) = \left\{ \begin{array}{c} -\boldsymbol{\varepsilon}_{n+1}^p + \boldsymbol{\varepsilon}_n^p + \Delta\gamma_{CC} \frac{\partial f_{CC}}{\partial \boldsymbol{\sigma}} \\ -\bar{I}_{1,n+1}^p + \bar{I}_{1,n}^p + \Delta\gamma_{CC} \frac{\partial f_{CC}}{\partial p} \\ \hline f_{CC} \end{array} \right\} = \mathbf{0} ,$$

with  $\mathbf{x} = [\boldsymbol{\varepsilon}_{n+1}^p, \bar{I}_{1,n+1}^p, \Delta\gamma_{CC}]^T$ . The matrix  $d\mathbf{R}/d\mathbf{x}$ , required for the solution of the Newton scheme becomes

$$(2.39) \quad \frac{d\mathbf{R}}{d\mathbf{x}} = \left[ \begin{array}{c|c} \mathbf{A}^{-1} & \nabla g_{CC} \\ \hline \nabla f_{CC}^T & 0 \end{array} \right] \left[ \begin{array}{cc|c} -\mathbf{C} & \mathbf{0} & \mathbf{0} \\ \mathbf{0}^T & -D & 0 \\ \hline \mathbf{0}^T & 0 & 1 \end{array} \right] ,$$

with  $D = -dq_{CC}/d\bar{I}_1^p$  and  $\mathbf{A}^{-1}$ ,  $\nabla f_{CC}$ , and  $\nabla g_{CC}$  are given as

$$(2.40) \quad \mathbf{A}^{-1} = \left[ \begin{array}{cc} \mathbf{C}^{-1} + \Delta\gamma_{CC} \frac{\partial^2 f_{CC}}{\partial \boldsymbol{\sigma}^2} & \Delta\gamma_{CC} \frac{\partial^2 f_{CC}}{\partial \boldsymbol{\sigma} \partial q_{CC}} \\ \Delta\gamma_{CC} \frac{\partial^2 f_{CC}}{\partial \boldsymbol{\sigma} \partial p} & D^{-1} + \Delta\gamma_{CC} \frac{\partial^2 f_{CC}}{\partial p \partial q_{CC}} \end{array} \right] ,$$

$$(2.41) \quad \nabla f_{CC} = \left\{ \begin{array}{c} \frac{\partial f_{CC}}{\partial \boldsymbol{\sigma}} \\ \frac{\partial f_{CC}}{\partial q_{CC}} \end{array} \right\} , \quad \nabla g_{CC} = \left\{ \begin{array}{c} \frac{\partial f_{CC}}{\partial \boldsymbol{\sigma}} \\ \frac{\partial f_{CC}}{\partial p} \end{array} \right\} .$$

The consistent tangent  $\mathbf{C}_{T,n+1} = d\boldsymbol{\sigma}_{n+1}/d\boldsymbol{\varepsilon}_{n+1}$  is obtained from extracting the respective submatrix from

$$(2.42) \quad \left\{ \begin{array}{c} d\boldsymbol{\sigma}_{n+1} \\ dq_{CC,n+1} \end{array} \right\} = \left[ \mathbf{A} - \frac{1}{g} \mathbf{A} \nabla g_{CC} \nabla f_{CC}^T \mathbf{A} \right] \left\{ \begin{array}{c} d\boldsymbol{\varepsilon}_{n+1} \\ 0 \end{array} \right\} ,$$

with

$$(2.43) \quad g = \nabla f_{CC}^T \mathbf{A} \nabla g_{CC} .$$

### *Extension to viscoplasticity*

For the nonlinear elastic Cam–Clay model, where the elastic domain is bounded by a single loading surface, the Perzyna-type of viscoplastic formulation is applied. Here, the evolution of the viscoplastic flow is obtained from Eq. (2.35) as

$$(2.44) \quad \dot{\boldsymbol{\varepsilon}}^{\text{vp}} = \frac{\langle f_{CC} \rangle}{\eta} \frac{\partial f_{CC}}{\partial \boldsymbol{\sigma}} \quad \text{and, thus,} \quad \dot{I}_1^{\text{vp}} = \frac{\langle f_{CC} \rangle}{\eta} \frac{\partial f_{CC}}{\partial p} ,$$

where  $\eta$  is the viscosity.

## **2.2. Material model for early-age cement-based materials**

Tunneling according to the NATM is characterized by a strong interaction between the hardening/creeping shotcrete shell and the viscous soil which exerts pressure on the lining. The creep properties of the shotcrete are the source of deformations required for the activation of load-carrying capacity of the surrounding soil formation. Both the shotcrete lining and, in case of ground improvement, the jet-grouted support ring are loaded during the hydration process.

In order to account for this chemomechanical coupling, a chemomechanical material model is used for the description of jet-grouted soil and shotcrete. Hereby, dissipative phenomena at the microlevel of the material are accounted for by means of the (internal) state variables and the energetically conjugate thermodynamic forces related to the state variables via the state equations. The rates of the internal state variables are related to the conjugate thermodynamic forces by means of evolution equations.

As is typical for cement-based materials, four dissipative phenomena govern the material behavior:

1. Hydration, resulting in chemical shrinkage strains, aging elasticity, and strength growth. The extent of the chemical reaction, i.e. of the hydration process, is described by the degree of hydration  $\xi$ , with  $0 \leq \xi \leq 1$ .
2. Microcracking of hydrates which are the result of the hydration process yields plastic strains  $\boldsymbol{\varepsilon}^p$ . The state of microstructural changes resulting from microcracking is described by hardening variables  $\boldsymbol{\chi}$ .
3. Stress-induced dislocation-like processes within the hydrates result in flow or long-term creep strains  $\boldsymbol{\varepsilon}^f$  [36]. The state of respective microstructural changes is described by the viscous flow  $\gamma$  [30].

4. Stress-induced microdiffusion of water in the capillary pores between the hydrates result in viscous or short-term creep strains  $\boldsymbol{\varepsilon}^v$  [24, 36, 30].

Table 1 contains the underlying field equations and constitutive relations of the employed material model. So-called intrinsic material functions, i.e. functions which do not depend on the field or boundary conditions, serve as input for the material model. Intrinsic material functions have been computed from slightly extended standard laboratory tests (see, e.g., [16, 26]). The intrinsic material

**Table 1. Governing equations for material model for shotcrete and jet-grouted soil.**

<b>FIELD EQUATIONS</b>	
<b>first law of thermodynamics</b> (see e.g.[31]):	$(\rho c)\dot{T} - \ell_\xi \dot{\xi} = -\text{div} \mathbf{q}$
<b>equilibrium condition:</b>	$\text{div} \boldsymbol{\sigma} + \mathbf{k} = \mathbf{0}$
<b>CONSTITUTIVE EQUATIONS</b>	
<b>heat conduction:</b> Fourier's law	$\mathbf{q} = -k \text{grad} T$
<b>incremental stress-strain law</b> [26]:	$d\boldsymbol{\sigma} = \mathbb{C}(\xi) : (d\boldsymbol{\varepsilon} - d\boldsymbol{\varepsilon}^p - d\boldsymbol{\varepsilon}^f - \alpha_T \mathbf{1} dT - \beta(\xi) \mathbf{1} d\xi - d\boldsymbol{\varepsilon}^v)$
<b>hydration kinetics</b> [32]: Arrhenius' law	$\dot{\xi} = \tilde{A}(\xi) \exp \left[ -\frac{E_a}{RT} \right]$
<b>microcracking</b> [15, 19]: multi-surface chemoplasticity	
admissible stress space:	$\boldsymbol{\sigma} \in C_E \Leftrightarrow f_\alpha \leq 0 \quad \forall \quad \alpha \in [DP, R1, R2, R3]$
loading surfaces:	$f_{DP} = \sqrt{J_2} + \alpha I_1 - \zeta_{DP}(\chi_{DP}, \xi)/\beta = 0$ $f_{RA} = \sigma_A - \zeta_R(\xi) = 0, \quad A = 1, 2, 3$
evolution equations:	$\dot{\boldsymbol{\varepsilon}}^p = \sum_{\alpha \in J_{\text{act}}} \dot{\gamma}_\alpha \partial_\sigma f_\alpha, \quad \dot{\chi}_{DP} = \dot{\gamma}_{DP} \partial_{\zeta_{DP}} f_{DP}$
Kuhn–Tucker conditions:	$f_\alpha \leq 0, \quad \dot{\gamma}_\alpha \geq 0, \quad f_\alpha \dot{\gamma}_\alpha = 0$
<b>short-term creep</b> [14]: aging viscoelastic law	
	$\dot{\boldsymbol{\varepsilon}}^v(t) = \frac{1}{\tau_w[\xi(t)]} \left[ \int_{t'=0}^t J_\infty^v[\xi(t')] \mathbb{G} : d\boldsymbol{\sigma}(t') - \boldsymbol{\varepsilon}^v(t) \right] \quad \text{with} \quad \mathbb{G} = \mathbb{C}^{-1} E$
<b>long-term creep</b> [2, 30, 26]:	
creep flow rule	$\dot{\boldsymbol{\varepsilon}}^f = \frac{1}{\eta_f} \mathbb{G} : \boldsymbol{\sigma}$
flow creep viscosity	$\frac{1}{\eta_f} = cS \exp \left[ -\frac{2U}{R} \left( \frac{1}{T} - \frac{1}{\bar{T}} \right) \right]$
microprestress force	$\dot{S} = -H\dot{\gamma}$
viscous slip rule	$\dot{\gamma} = cS^2 \exp \left[ -\frac{U}{R} \left( \frac{1}{T} - \frac{1}{\bar{T}} \right) \right]$

functions used in the following study are defined by the parameters given in Tables 2 and 3.

For a more detailed description of the chemomechanical material model employed in this paper, the reader is referred to [16, 26, 14, 19].

**Table 2. Material parameters employed for the numerical simulation of NATM tunneling in granular soil (see [26, 14] for shotcrete, [22, 7] for jet-grouted soil, and [1] for sand).**

chosen set of material parameters for sand, jet-grouted soil, and shotcrete			
	sand	jet-grouted soil	shotcrete
unit weight of material, $\gamma$ [MN/m <sup>3</sup> ]	0.017	0.021	0.025
(final) Young's modulus, $E$ [MPa]	45	1 500	40 800
Poisson's ratio, $\nu$ [-]	0.35	0.2	0.2
initial friction angle, $\varphi_i$ [°]	20	–	–
peak friction angle, $\varphi_p$ [°]	30	–	–
cohesion, $c$ [MPa]	0.001	–	–
initial dilation angle, $\psi_i$ [°]	0	–	–
peak dilation angle, $\psi_p$ [°]	4	–	–
internal variable $\chi_{MC}$ at $\varphi = \varphi_p$ , $\chi_{MC,m}$ [-]	0.03	–	–
fluidity parameter, $\tau$ [h]	0.15	–	–
compressive strength, $f_{c,\infty}$ [MPa]	–	8.0	39.6
percolation threshold, $\xi$ [-]	–	0.5	0.01
elastic limit, $f_{c,y}$ [MPa]	–	$f_c/4$	$f_c/4$
tensile strength, $f_t$ [MPa]	–	$f_c/10$	$f_c/10$
$f_b/f_c$ [-]	–	1.16	1.16
relaxation modulus $H$ [MPa]	–	$1 \cdot 10^6$	$1/7 \cdot 10^6$
total strain at peak load, $\varepsilon_m$ [-]	–	-0.0022	-0.0022
shrinkage parameter $\beta = a_s + b_s \xi$	–	–	–
$a_s$ [-]	–	$-4.05 \cdot 10^{-4}$	$-4.05 \cdot 10^{-4}$
$b_s$ [-]	–	$9.43 \cdot 10^{-4}$	$9.43 \cdot 10^{-4}$
asymptotic viscous compliance $J_\infty^v = a_v(1 - \xi)$	–	–	–
$a_v$ [ $\mu\text{m}/(\text{m MPa})$ ]	–	148.5	445
characteristic time for short-term creep $\tau_w$ [h]	–	48	48
activation term $U/R$ [K]	–	2 700	2 700
reference temperature $\bar{T}$ [°C]	–	20	20
activation term $E_a/R$ [K]	–	4 000	4 000
chemical affinity $\tilde{A} = a_A \frac{1 - \exp(-b_A \xi)}{1 + c_A \xi^{d_A}}$	–	–	–
$a_A$ [1/s]	–	8.24	7.31
$b_A$ [-]	–	13.3	10.5
$c_A$ [-]	–	117.0	169.0
$d_A$ [-]	–	6.63	4.37
temperature $T_0$ [°C]	10	20	20

**Table 3.** Material parameters employed for the numerical simulation of NATM tunneling in cohesive soil (see [26, 14] for shotcrete, [12, 7] for jet-grouted soil, and [25] for clay).

chosen set of material parameters for clay, jet-grouted soil, and shotcrete			
	clay	jet-grouted soil	shotcrete
unit weight of material, $\gamma$ [MN/m <sup>3</sup> ]	0.0235	0.017	0.02428
(final) Young's modulus, $E$ [MPa]	–	550	40 800
Poisson's ratio, $\nu$ [–]	–	0.2	0.2
slope of the normal compression line, $\lambda$ [–]	0.161	–	–
slope of the unloading-reloading line, $\kappa$ [–]	0.062	–	–
slope of the critical state line, $M$ [–]	0.88	–	–
initial specific volume, $v_0$ [–]	2	–	–
initial size of the elastic domain, $q_0$ [MPa]	0.80	–	–
tensile strength, $t$ [MPa]	0.23	–	–
amount of coupling in elasticity, $\tilde{\alpha}$ [–]	15	–	–
viscosity of the soil, $\eta$ [MPa·h]	3	–	–
compressive strength, $f_{c,\infty}$ [MPa]	–	2.5	39.6
percolation threshold, $\xi$ [–]	–	0.5	0.01
elastic limit, $f_{c,y}$ [MPa]	–	$f_c/4$	$f_c/4$
tensile strength, $f_t$ [MPa]	–	$f_c/10$	$f_c/10$
$f_b/f_c$ [–]	–	1.16	1.16
relaxation modulus $H$ [MPa]	–	$1 \cdot 10^6$	$1/7 \cdot 10^6$
total strain at peak load, $\varepsilon_m$ [–]	–	–0.0022	–0.0022
shrinkage parameter $\beta = a_s + b_s \xi$	–	–	–
$a_s$ [–]	–	$-4.05 \cdot 10^{-4}$	$-4.05 \cdot 10^{-4}$
$b_s$ [–]	–	$9.43 \cdot 10^{-4}$	$9.43 \cdot 10^{-4}$
asymptotic viscous compliance $J_\infty^v = a_v(1 - \xi)$	–	–	–
$a_v$ [ $\mu\text{m}/(\text{m MPa})$ ]	–	148.5	445
characteristic time for short-term creep $\tau_w$ [h]	–	48	48
activation term $U/R$ [K]	–	2 700	2 700
reference temperature $\bar{T}$ [°C]	–	20	20
activation term $E_a/R$ [K]	–	4 000	4 000
chemical affinity $\tilde{A} = a_A \frac{1 - \exp(-b_A \xi)}{1 + c_A \xi^{d_A}}$	–	–	–
$a_A$ [1/s]	–	8.24	7.31
$b_A$ [–]	–	13.3	10.5
$c_A$ [–]	–	117.0	169.0
$d_A$ [–]	–	6.63	4.37
temperature $T_0$ [°C]	10	20	20

### 3. Presentation of results

Two example problems considering tunneling situations characterized by low overburden are investigated. The first example deals with the effectiveness of support means under different geological conditions. In the second example, the influence of the primary conditions on the structural response during the excavation is investigated.

### 3.1. Example 1: Effectiveness of support means for tunneling in different types of soil

As the first example problem, a tunneling situation characterized by low overburden is chosen. The surrounding soil is modelled as a homogeneous material, consisting of either medium-dense sand or soft clay (see Tables 2 and 3). With regards to these ground conditions, a three-step excavation scheme consisting of top heading, benches and invert is considered in the numerical simulation. After each excavation step, application of shotcrete onto the tunnel walls is simulated by changing the material description from soil to shotcrete in the finite elements representing the lining. According to [6], this change results in negligibly small strength and stiffness of the grouted material. Since the original microstructure of the soil is destroyed during jet grouting, disregard of strength and stiffness of the young jet-grouted soil mass is appropriate. Additionally, ground improvement by means of horizontal jet grouting (HJG) is considered<sup>2)</sup> (see Fig. 5). The properties of jet-grouted soil depend on the amount of injected cement grout which, on the other hand, depends on the *in-situ* soil.

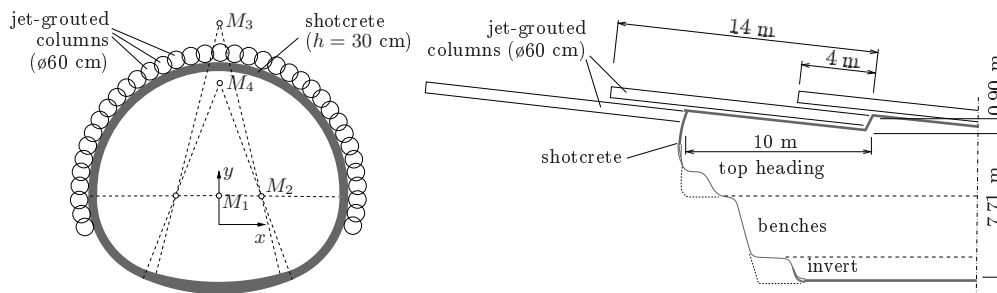


FIG. 5. Adopted tunnel excavation situation.

In case of granular material, the cement grout mixes with the soil particles, giving mechanical properties close to mortar. During jet grouting in clays, on the other hand, the soil is almost replaced by the injected cement grout. Accordingly, in this case both the compressive strength  $f_c$  and Young's modulus  $E$  at the end of hydration ( $t = \infty$ ) were set equal to the respective values of cement paste. Generally, an increase of the hydrostatic pressure in the soil during jet grouting may be considered by adding a hydrostatic stress state  $\Delta p$  to the initial stress state after jet grouting. The latter results from dead load of the jet-grouted soil mass. In what is called compensation grouting, this hydrostatic pressure

<sup>2)</sup>During HJG, slightly inclined holes, drilled from the tunnel face, are used for high-pressure injection of cement grout, finally giving a cone-shaped support ring consisting of cemented soil ahead of the tunnel face.

is increased by preventing backflow of the grouting material through the bore hole. The increased hydrostatic pressure results in heaving of the surface which “compensates” settlements caused by the tunnel excavation [9, 10]. At the tunnel site investigated in this section, however, compensation grouting shall not be considered. Accordingly,  $\Delta p$  can be set equal to zero. Therefore, the numerical results reported in this section represent the upper limit of the settlements caused by jet grouting. Furthermore, as the supporting face effect is disregarded in the performed plane strain simulations, the numerically obtained settlements are expected to be higher. Hence, these results represent the worst case.

Altogether four numerical Finite Element simulations were performed, covering tunnel excavation with and without HJG in medium-dense sand and clay. Based on the obtained numerical results, the following questions arising from the application of different support means in NATM tunneling in different geological conditions are posed:

*Does the local destruction of the soil microstructure during jet grouting result in settlements which finally, after tunnel excavation, give larger settlements compared to the tunnel excavation without ground improvement?*

Standardly, the construction of the jet-grouted support is optimized in order to minimize these pre-excitation settlements by avoiding fresh-to-fresh jet-grouted columns (see [22]). In [21] it was shown that the horizontal dimension of the jet-grouted support defines the amount of settlements associated with the ground-improvement work. In certain cases, limitation of ground improvement to the benches, characterized by a rather small horizontal dimension of the jet-grouted support, yields less total settlements (resulting from jet grouting *and* excavation) than the tunnel excavation supported by an entire jet-grouted support ring. In the present study, where a support ring consisting of 37 columns was considered, the settlements associated with ground improvement amounted to 23 mm and 31 mm for jet grouting in sand and clay, respectively. The higher settlements for the clay, especially when jet grouting near the top heading is performed (for the construction scheme of the jet-grouted support, see [22]), can be explained by the higher dead load of the clay (see Tables 2 and 3) and the lower initial strength and stiffness of the early-age jet-grouted clay.

Even though the final settlements obtained from the analyses disregarding jet grouting, taking only the interaction between the creeping soil and the hydrating shotcrete lining into account, are almost equal<sup>3)</sup>, the settlements obtained from

---

<sup>3)</sup>For both soils considered in this study, the time scales associated with creep were set equal. Accordingly, for a characteristic time  $\tau$  for the sand equal to  $\tau_{\text{sand}} = 0.15$  h, the viscosity  $\eta$  of the clay is obtained from  $\tau_{\text{clay}} = \eta_{\text{clay}} / \tilde{E}_{\text{clay}} \stackrel{!}{=} \tau_{\text{sand}}$ , where  $\tilde{E}_{\text{clay}}$  is the Young’s modulus for a stress state characterized by 20 m overburden and a lateral pressure coefficient of 0.5, giving  $\eta_{\text{clay}} = 0.15 \cdot 20 = 3$  MPa h. However, in addition to the characteristic time  $\tau$  for

the analyses considering HJG are quite different (see Fig. 6). On the one hand, this difference is explained by the different mechanical properties of jet-grouted clay and sand. On the other hand, as will be described later, inelastic deformations in the soil adjacent to the jet-grouted support lead to different deformation pattern of the tunnel opening, yielding less convergence and higher settlements for the tunnel excavation in clay.

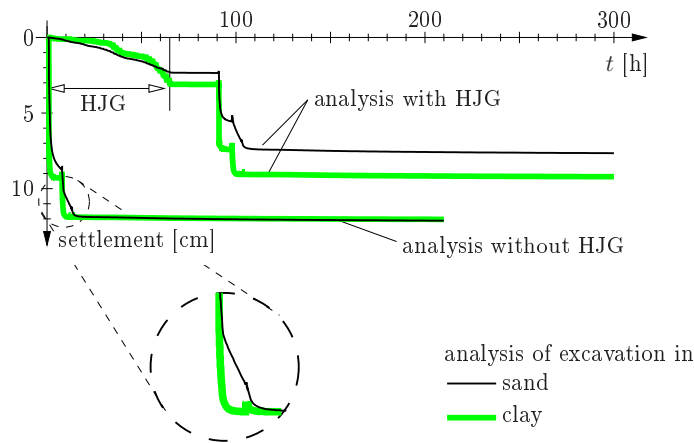


FIG. 6. History of surface settlements above crown

Compared to tunnel excavation considering a shotcrete support only, HJG led to a reduction of the final settlements by 33% in sand and by 25% in clay, justifying the application of ground improvement techniques within the considered three-step excavation scheme, especially for tunneling in urban areas.

*How do the support means influence the convergence history measured on site and does the latter provide insight into the structural performance of the support means?*

As mentioned in Sec. 1, adaptation of support means in NATM tunneling is based on *in-situ* measurements. Hence, the question of how the obtained measurements change when new structural components such as jet-grouted support are introduced, is of prime interest in the day-to-day decision process. Whereas the horizontal convergence depicted in Fig. 7 gives similar results for the analy-

---

the creep process, the direction of plastic flow influences the time scale of the displacement history at the structural scale. E.g., the deformation in sand, where the plastic flow (dilation) strongly deviates from the stress paths associated with confined compressive stress states, the structural response is significantly delayed (see Fig. 6). Thus, the almost equal values for the final displacements in tunneling in sand and clay obtained from the analyses disregarding HJG are rather a coincidence than a consequence of the time scales for creep in soil, chosen to be equal for sand and clay.

ses disregarding HJG, it differs significantly when jet grouting is taken into account. Concentrating on the evolution of the horizontal convergence for  $t > 91$  h (for  $t < 91$  h, the convergence takes place in the improved ground and, hence, cannot be accessed on site), the structural support provided by the jet-grouted support ring led to a reduction of the convergence. Whereas the dilation associated with direction of plastic flow of the Mohr–Coulomb criterion still leads to convergence during tunnel excavation, the confined compressive stress states in the clay close to the jet-grouted support at the benches result in compaction (associative flow rule was adopted for the Cam–Clay criterion), yielding a further decrease of the convergence.

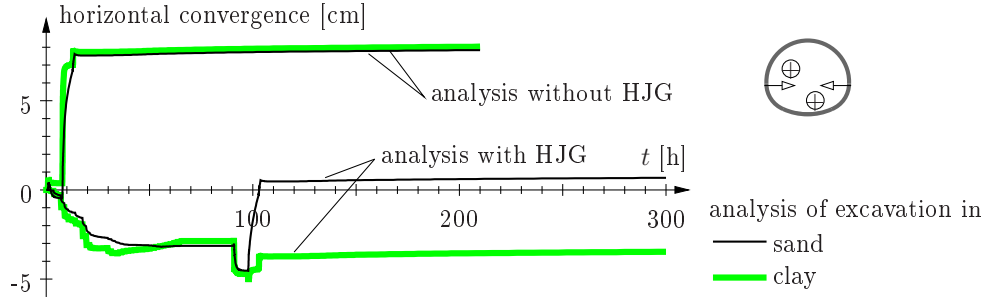


FIG. 7. History of horizontal convergence.

*How do the geological conditions and support means influence the loading characteristics of the soil-support composite structure?*

Whereas similar values for the final settlements were obtained for both types of soil in the analyses disregarding HJG, the loading of the shotcrete lining is significantly different. Since the structural creep process in clay is considerably shorter (see Fig. 6), the lining becomes loaded when the strength properties of shotcrete are less developed, mainly resulting in inelastic deformations. As the strength of the hydrating shotcrete lining increases with time, the creep process in the sand, which is significantly slower than the one in clay, results in higher loading of the lining (Fig. 8(a)). Application of HJG yields a composite-shell structure consisting of the jet-grouted support and the shotcrete lining. Accordingly, bending results in an increase of the hoop force in the shotcrete lining while the hoop force drops in the jet-grouted support, and vice versa. This effect is more pronounced during tunneling in clay, where plastic compaction of the adjacent soil provides the flexibility required for bending, resulting even in tensile loading of the lining (see Fig. 8(b)). As regards tunneling in medium-dense sand considering HJG, the confinement associated with plastic dilation preserves the compressive stress state in the lining. Because of this, the compressive hoop

force in the lining for tunnel excavation in sand is greater in each shell section than the respective force obtained from tunneling in clay.

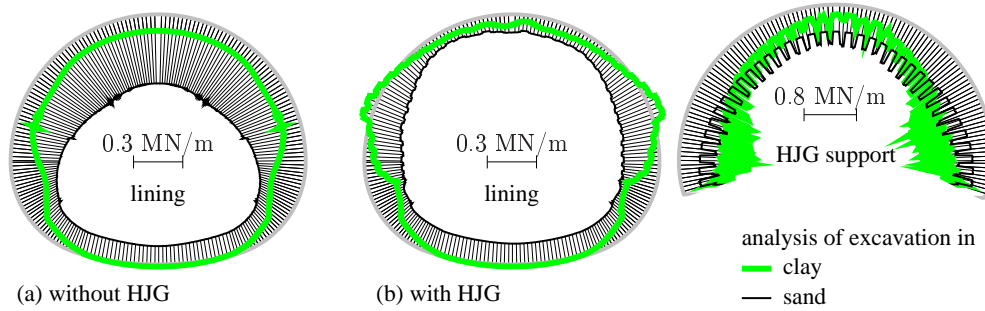


FIG. 8. Distribution of hoop force (a) in the lining when HJG is disregarded, and (b) in the lining and the jet-grouted support when HJG is considered (plots give hoop force 7 days after excavation of the invert).

### 3.2. Example 2: Influence of primary conditions on structural response during excavation

For this example, tunneling in cohesive soil (see properties of clay given in Table 4), characterized by an overburden of about one tunnel diameter, is investigated. The geometric dimensions of the tunnel cross-section are given in Fig. 9. Similar to Example 1, an excavation scheme characterized by subsequent excavation of the heading, the benches, and the invert is employed. The time interval between two subsequent excavation steps is set equal to  $t = 120$  h.

The primary stress state is given by the vertical stress  $\sigma_v = \gamma \cdot z$ , where  $z$  represents the distance from the surface, and the horizontal stress  $\sigma_h = K_0 \cdot \sigma_v$ , with  $K_0$  as the ratio of the horizontal to the vertical stress. Accordingly,

Table 4. Material parameters for clay.

unit weight of material, $\gamma$ [MN/m <sup>3</sup> ]	0.0235
slope of the normal compression line, $\lambda$ [-]	0.040
slope of the unloading-reloading line, $\kappa$ [-]	0.008
initial size of the elastic domain, $q_0$ [MPa]	0.80
slope of the critical state line, $M$ [-]	0.61
tensile strength, $t$ [MPa]	0.22
initial specific volume, $v_0$ [-]	1.30
amount of coupling in elasticity, $\tilde{\alpha}$ [-]	100.0
viscosity $\eta$ [MPa h]	200
linear elastic parameters for $K_0 = 0.66$	
bulk modulus, $K$ [MPa]	94
shear modulus, $G$ [MPa]	57

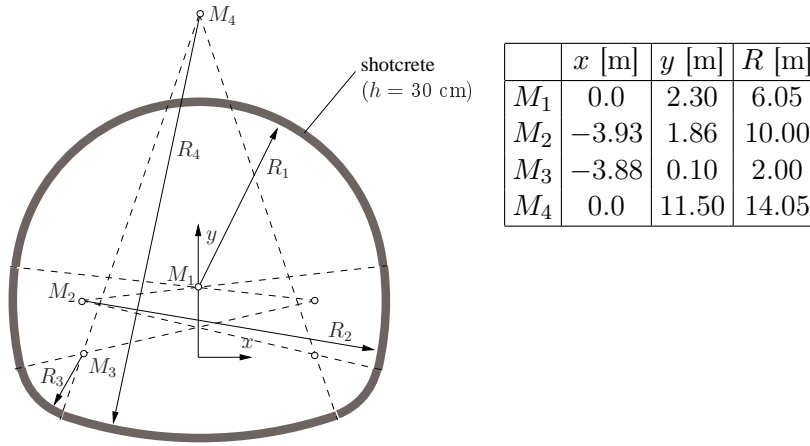


FIG. 9. Geometric dimensions of tunnel cross-section.

for increasing values of  $z$ , the stress state approaches the yield function of the underlying Cam–Clay model  $f(\boldsymbol{\sigma}, q_0) = 0$ , with the value of  $q_0$  given in Table 4. Below a certain depth in the soil, the stress state even violates the yield criterion  $f(\boldsymbol{\sigma}, q_0) \leq 0$ . In this area, the internal variables and, thus, the yield surface are adapted such that the initial stress state yields  $f(\boldsymbol{\sigma}, q) = 0$ , with  $q \geq q_0$ . As recent publications indicate [5, 13], there is no consensus on the description of the elastic behavior in elastoplastic processes in soils. In order to assess the effect of nonlinear-elasticity (NLE) models compared to linear elasticity (LE) for tunneling processes, plane strain FE analyses are performed, using either the underlying nonlinear-elasticity formulation of the Cam–Clay model or a linear-elasticity model. As regards the latter, the values of the bulk modulus  $K$  and the shear modulus  $G$  were determined from the elasticity matrix  $\mathbf{C}$  obtained from the nonlinear-elasticity model for the respective primary stress state for a depth of 20 m. First, the shear modulus is obtained from  $G = (C_{44} + C_{55} + C_{66})/3$ . Then, based on that value of  $G$ , the bulk modulus  $K$  is determined from the average value of the three off-diagonal terms  $C_{12}, C_{13}$ , and  $C_{23}$ , reading  $(C_{12} + C_{13} + C_{23})/3 = K - 2/3G$ .

#### *Effect of lateral earth pressure*

In order to investigate the influence of the lateral earth pressure, the tunneling process was investigated for three different values of  $K_0$ , with  $K_0 = 0.1, 0.5$ , and  $0.9$ . The locations of the initial stress states corresponding to the different values of  $K_0$  are shown in Fig. 10 for  $z = 10, 20$ , and  $40$  m. For  $K_0 = 0.1$ , the stress state is located above the *critical state line* (i.e., in the softening regime), whereas for  $K_0 = 0.9$ , the stress state is located below the *critical state line* (i.e., in the hardening regime). In addition to the location of the initial stress state with

respect to the *critical state line*, the adaptation of the internal variable  $q$  of the Cam–Clay criterion to the initial stress gives a larger elastic domain as the value of  $K_0$  decreases (see the size of the yield surfaces in Fig. 10 for stress state at 20 m depth for  $K_0 = 0.1, 0.5$ , and  $0.9$ ). The bulk modulus and the shear modulus for the different values of  $K_0$  are determined from the nonlinear-elasticity model considering the stress state at  $z = 20$  m, with  $\sigma_v = 0.0235 \cdot 20 = 0.47$  MPa and  $\sigma_h = K_0 \cdot \sigma_v$ .

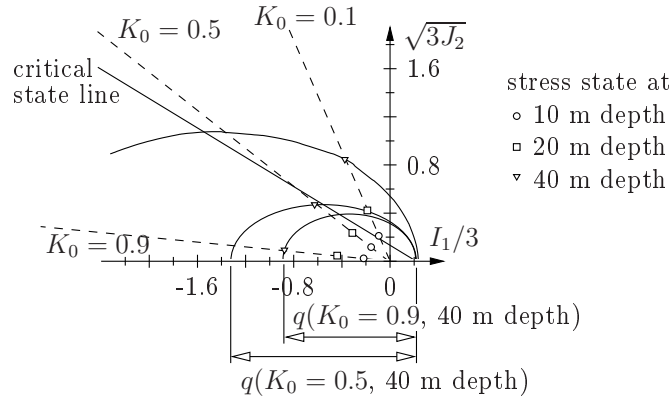


FIG. 10. Initial stress state at 10, 20, and 40 m depth for different values of  $K_0$ .

The numerically-obtained displacement at the top of the tunnel cross-section is given in Fig. 11, which becomes larger as the value of  $K_0$  increases from 0.1 to 0.5. As the value of  $K_0$  is further increased, however, smaller vertical displacements at the top of the tunnel were obtained. This change of trend is a consequence of two counteracting processes:

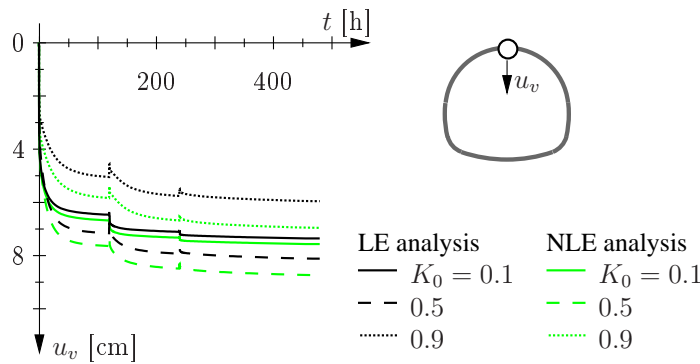


FIG. 11. Evolution of vertical displacement at the top of the tunnel cross-section for different values of  $K_0$  for linear elasticity (LE) and nonlinear elasticity (NLE), respectively.

1. *Surrounding soil as a load-carrying structure:* For small values of  $K_0$  and, thus, small values for the initial horizontal stress, a load-carrying arch (protection zone) in the surrounding soil cannot be formed. This results in a vertical movement of the soil masses above the tunnel opening (inducing bending moments in the load-carrying shotcrete lining). As the value of  $K_0$  increases, however, the protection zone around the tunnel opening starts to establish. The combined load-carrying soil-arch – shotcrete-lining support structures leads to a reduction of the vertical displacement of the tunnel crown (see also deformation plots in Fig. 12).

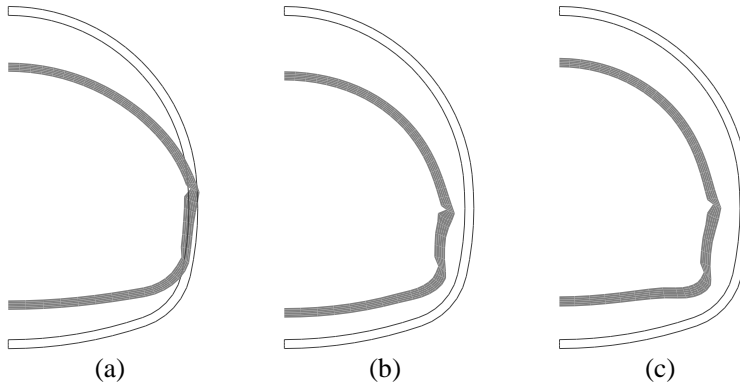


FIG. 12. Deformation of the shotcrete shell (25-fold magnification) at  $t = 480$  h for NLE analysis and (a)  $K_0 = 0.1$ , (b)  $K_0 = 0.5$ , and (c)  $K_0 = 0.9$ .

2. *Plastic dilation/contraction:* As mentioned earlier, the value of  $K_0$  defines the location of the initial stress state with respect to the critical state line. For large values of  $K_0$ , the initial stress states are found below the critical state line, giving, in case of plastic loading, a contracting material behavior. This type of behavior results in increased flexibility of the support means (shotcrete lining) and, thus, in large vertical displacements, especially at the footing of the top heading, where the load of the lining is transferred into the ground. For small values of  $K_0$ , on the other hand, the initial stress states are found above the critical state line. The so-obtained dilating behavior in case of plastic loading leads to an increase of the confinement in the soil supporting the shotcrete lining and, hence, to smaller vertical displacements.

For  $K_0 = 0.1$  and  $0.9$  either one of the two mentioned processes becomes dominant, resulting in a reduction of the vertical displacement as depicted in Fig. 11. For  $K_0 = 0.5$ , the positive effect of these processes on the reduction of the vertical displacement is not fully activated. Accordingly, the largest vertical displacement was obtained for this value of  $K_0$ . The almost instantaneous re-

duction of the vertical displacement right after the excavation of the bench and the invert observed in Fig. 11 results from the horizontal inward movement of the benches, leading to heave of the crown.

Comparing the numerical results obtained from NLE and LE analysis, the influence of the underlying elasticity model increases with increasing  $K_0$  (see Fig. 11). This trend is linked to the initial hydrostatic stress in the soil, which, for the Cam–Clay model, defines the values of the stiffness properties. For small values of  $K_0$ , the initial hydrostatic stress in the soil, with  $I_1 = (2K_0 + 1) \cdot \gamma \cdot z$ , changes little with depth. This gives NLE stiffness properties close to the LE stiffness parameters ( $K$  and  $G$ , corresponding to the NLE properties at  $z = 20$  m). As the value of  $K_0$  increases, the variation of  $I_1$  over the depth increases, resulting in a larger deviation between the NLE and LE properties. This explains the larger deviations of NLE from LE analysis results for  $K_0 = 0.9$ . As the values of the NLE stiffness parameters are smaller than the respective values for the LE model for depths  $0 \leq z \leq 20$  m, i.e., where most of the soil loading takes place, larger values for the vertical displacement were obtained from the NLE analyses.

### *Effect of overconsolidation ratio $R$*

So far, the primary stress state of the soil was determined from the ratio of horizontal to vertical stress,  $K_0$ , giving initial stress states either inside the elastic domain, with  $f(\boldsymbol{\sigma}, q_0) < 0$ , or, in case of violation of the yield criterion, on the (adapted) yield surface, with  $f(\boldsymbol{\sigma}, q > q_0) = 0$ . In this study, the initial value of the Cam–Clay parameter  $q$  is increased by a so-called overconsolidation ratio  $R$ , with the yield criterion reading  $f(\boldsymbol{\sigma}, R \cdot q) \leq 0$ . Thus, initially elastic material response will occur in the course of tunnel excavation. For this study,  $K_0$  was obtained from Jaky's theory, with

$$(3.1) \quad K_0 = \frac{\sigma_h}{\sigma_v} = 1 - \sin \varphi .$$

Hereby, the friction angle  $\varphi$  is related to the slope of the *critical state line*  $M$ , reading [37]

$$(3.2) \quad \sin \varphi = \frac{3M}{6 - M} = \frac{3 \cdot 0.61}{6 - 0.61} \quad \rightarrow \quad \varphi \approx 20^\circ .$$

In Eq. (3.2), the tensile meridian of the respective Mohr–Coulomb criterion was used. From Eq. (3.1) and  $\varphi = 20^\circ$ ,  $K_0$  is given by  $K_0 = 0.66$ .

The numerical results obtained from  $R = 1.1, 1.5$ , and  $2.0$  are depicted in Fig. 13. Again, both elasticity models (NLE and LE) were considered. The parameters for the LE analyses were obtained from  $\sigma_v = 0.47$  MPa and  $K_0 = 0.66$  (see Table 4). With increasing values of  $R$ , the soil response during the excavation is increasingly dominated by elastic material behavior, resulting in lower

displacements. E.g., for  $R = 2.0$  the instantaneous heave of the top of the tunnel from inward movement of the benches for bench and invert excavation almost compensates the subsequent displacements in consequence of the creep of soil. This rather small amount of creep deformation gives marginal stress redistribution from the creeping soil to the hydrating shotcrete lining, explaining the small values for the hoop force depicted in Fig. 14. For a small value of  $R$ , on the other hand, the displacements associated with creep of the soil become larger, resulting in increased loading of the lining. Finally, the installation of the invert and, thus, the closure of the shotcrete support ring reduces the displacement rate. This shows the stabilizing effect of ring closure.

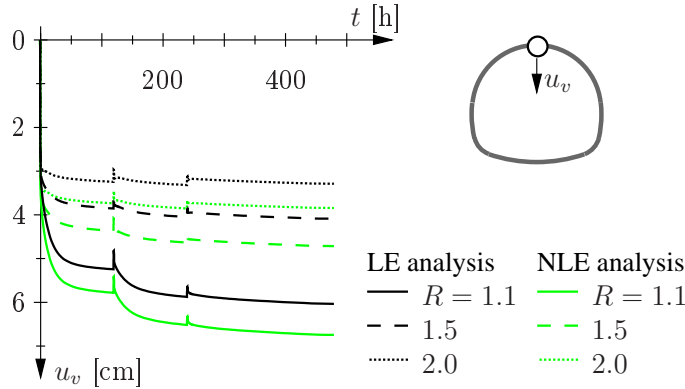


FIG. 13. Evolution of vertical displacement at the top of the tunnel cross-section for different values of  $R$  for linear elasticity (LE) and nonlinear elasticity (NLE), respectively.

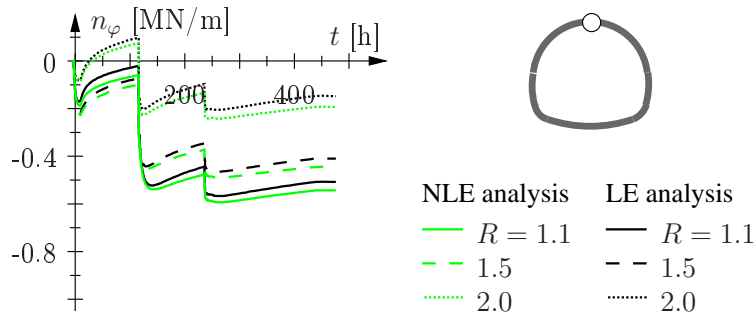


FIG. 14. Evolution of hoop force in the shotcrete lining at the top of the tunnel cross-section for different values of  $R$  for linear elasticity (LE) and nonlinear elasticity (NLE), respectively.

Similar to the previous study, the NLE formulation, what is less stiff in comparison to the (constant) elasticity parameters  $K$  and  $G$  of the LE formulation for  $0 \leq z \leq 20$  m, gives larger vertical displacements for the NLE analyses. Since

the initial stress state and, thus, the initial NLE stiffness properties are the same for all the analyses, the value of  $R$  has only little influence on the NLE and LE displacement.

#### *Effect of soil viscosity $\eta$*

The success of the NATM strongly depends on the interaction of the creeping soil and the hydrating shotcrete lining. In order to assess the influence of the viscous properties of the soil, three analyses with  $\eta = 20, 200,$  and  $2000$  MPa h were performed. The characteristic time of the creep process in the soil is estimated by  $\tau = \eta/E$ , where  $E$  represents the Young's modulus and is determined from the elasticity parameters  $K$  and  $G$  (see Table 4) of the LE analysis as

$$(3.3) \quad E = \frac{9KG}{3K + G} \approx 140 \text{ MPa} ,$$

giving  $\tau = 0.14, 1.4,$  and  $14$  h. Taking the effect of the underlying flow rule on the structural creep process into account, the time scale of the structural creep response,  $\tau_s$ <sup>4</sup>, is close to the characteristic time  $\tau_h = 41.5$  h of the shotcrete hydration process, highlighting the importance of ground-lining interaction in NATM tunneling. Hereby,  $\tau_h$  was related to the maximum slope in the evolution of the hydration degree  $\xi$  [33]. In case of isothermal conditions with  $T = 293$  K and  $E_a/R = 4000$  K [11], this slope is obtained from

$$(3.4) \quad \max \left\{ \frac{d\xi}{dt} \right\} = \max \left\{ \tilde{A}(\xi) \right\} \exp \left( -\frac{E_a}{RT} \right) ,$$

giving  $\tau_h$  as

$$(3.5) \quad \tau_h = \frac{1}{\max\{d\xi/dt\}} = \frac{1}{\max\{\tilde{A}(\xi)\}} \exp \left( \frac{E_a}{RT} \right) \\ = \frac{1}{5.68 \times 3600} \exp \left( \frac{4000}{293} \right) = 41.5 \text{ h} .$$

In Eq. (3.5), the chemical-affinity function  $\tilde{A}(\xi)$  for shotcrete was taken from [22]. The numerically-obtained vertical displacement at the top of the tunnel is shown in Fig. 15. For large values of the viscosity, the delay in the inward movement of the soil provides time for the hydration of the shotcrete lining and for the increase of its stiffness and strength. The latter results in more resistance against the ground movement, leading to less vertical displacements as depicted in Fig. 15.

<sup>4</sup>The value of  $\tau_s$  was determined for a Drucker–Prager type soil model as  $100\tau$  (plane-strain 2D analysis [17]) and  $50\tau$  (axisymmetric 2D analysis [3]), see also Example 1.

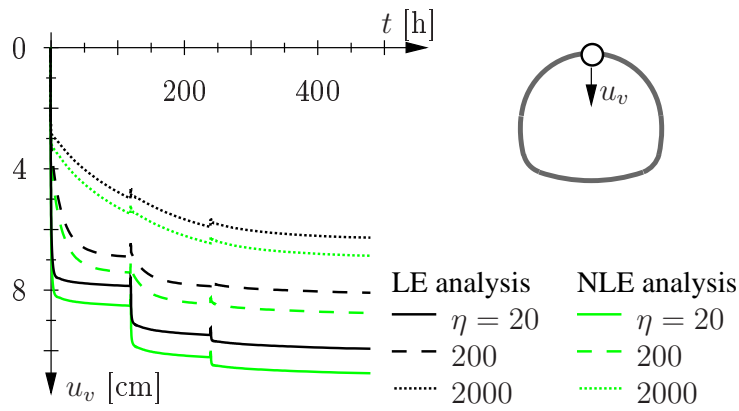


FIG. 15. Evolution of vertical displacement at the top of the tunnel cross-section for different values of  $\eta$  for linear elasticity (LE) and nonlinear elasticity (NLE), respectively.

As the viscosity of the soil decreases, the characteristic time of creep of soil becomes significantly smaller than the characteristic time of the hydration process, resulting in fast development of soil deformation and, thus, loading of the young shotcrete lining. Right after installation of the top heading, this causes plastic deformations in the lining, giving similar values for the hoop force (see Fig. 16). The observed decrease of the hoop force after each excavation step for the analyses with  $\eta = 20$  and 200 MPa h is explained by the vertical displacement of the tunnel crown, inducing bending and, thus, tensile loading at the top of the lining. A large soil viscosity, on the other hand, results in a slow stress redistribution and, hence, in a continuous increase of the hoop force (see analyses with  $\eta = 2000$  MPa h in Fig. 16).

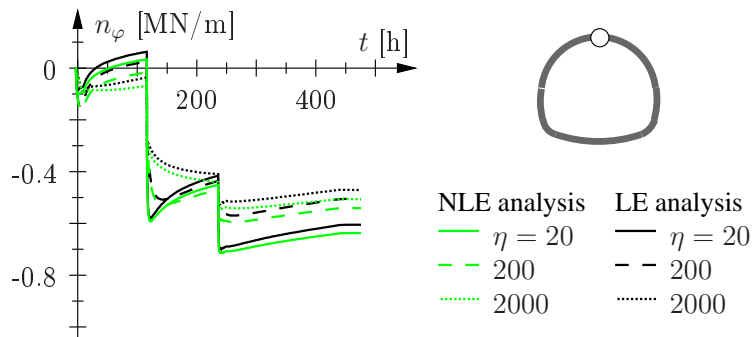


FIG. 16. Evolution of hoop force in the shotcrete lining at the top of the tunnel cross-section for different values of  $\eta$  for linear elasticity (LE) and nonlinear elasticity (NLE), respectively.

In spite of the smaller displacements obtained for larger values of the soil viscosity (Fig. 15), the final hoop force of the lining (Fig. 16) is quite similar for the different values of  $\eta$ . Whereas for an unlined excavation process the final displacement is the same for different soil viscosities, reached at different time instants, the interaction between the creeping soil and the hydrating shotcrete lining explains the slight variations of the hoop force at  $t = 480$  h.

#### 4. Concluding remarks

Based on the numerical analysis scheme employed in this paper, considering the complex construction process of NATM tunneling and accounting for the time-dependent behavior of the involved materials, the effect of support means for tunneling under different geological conditions and the influence of changes of these geological conditions were highlighted.

The numerical results presented in the first example indicated a strong influence of the time scale of the structural deformation process on the loading of the support means. E.g., even though similar settlements were obtained for tunneling in sand and clay, the loading of the lining was significantly different. Therefore, numerical studies are indispensable to obtain information not accessible by measurements, such as the loading of the support means and, equally important, the effectiveness of the adaptation of support means. The latter provides (1) essential input for the day-to-day decision process at the construction site and (2) information on the changes to be expected in the displacement history as the mode of adaptation has been specified.

The numerical results obtained from the second example highlighted the large influence of changes of the geological conditions on the structural response. Hereby, the history of the vertical displacement and the hoop force in the lining were determined for different values of the lateral stress, of the so-called overconsolidation ratio, and of the soil viscosity. Any changes in one of these geological conditions alters the stress redistribution from the creeping soil towards the hydrating lining. These alterations not only have an influence on the amount of displacement and loading, but also on the time scale of the stress redistribution process. Hence, a change of geological conditions affects the data monitored in the course of excavation processes. In contrast to the first example dealing with different support means, the second example gave access to changes in monitoring data in consequence of changing the soil conditions. Both types of information are essential in understanding the data monitored at tunnel-construction sites and enlarge the basis for the day-to-day decision process in NATM tunneling.

## References

1. J.P. BARDET, *Experimental soil mechanics*, Prentice Hall, New Jersey 1997.
2. Z.P. BAŽANT, A.B. HAUGGARD, S. BAWEJA, and F.-J. ULM, *Microprestress solidification theory for concrete creep, part I: Aging and drying effects*. *Journal of Engineering Mechanics*, ASCE, **123**, 11, 1188–1194, 1997.
3. D. BOLDINI, R. LACKNER, and H.A. MANG, *Ground-shotcrete interaction of NATM tunnels with high overburden*, *Journal of Geotechnical and Geoenvironmental Engineering* (ASCE), **131**, 7, 2005.
4. R.I. BORJA, R.A. REGUEIRO, and T.Y. LAI, *FE modelling of strain localization in soft rock*, *Journal of Geotechnical and Geoenvironmental Engineering*, **126**, 4, 335–343, 2000.
5. R.I. BORJA and C. TAMAGNINI, *Numerical implementation of a mathematical model for finite strain elastoplastic consolidation*, [in:] D.R.J. OWEN, E. OÑATE, and E. HINTON, [Eds.], *Computational Plasticity*, Proceedings of the 5-th International Conference, 1631–1640, CIMNE, Barcelona 1997.
6. CH. BRANDSTÄTTER, R. LACKNER, and H.A. MANG, *Evaluation of properties of cementitious materials by means of temperature measurements: Application to jet grouting* [in German], *Bauingenieur*, **77**, 2, 51–57, 2002.
7. CH. BRANDSTÄTTER, R. LACKNER, CH. PICHLER, and H.A. MANG, *Application of jet grouting in NATM tunneling*, [in:] S. VALLIAPPAN *et al.*, [Ed.], *Proceedings of the 1-st Asian Pacific Congress on Computational Mechanics*, Sydney, Australia 2001.
8. G. DUVAUT and J.L. LIONS, *The inequalities in mechanics and physics* [in French], Dunod, Paris 1972.
9. E. FALK, *Underground works in urban environment*, [in:], *Proceedings of the 14-th International Conference on Soil Mechanics and Foundation Engineering*, **3**, 1401–1406, Hamburg, Germany, 1997. Balkema Rotterdam.
10. E. FALK, *Compensation grouting – State of the art in tunneling* [in German], [in:] H. BRANDL [Ed.], *Proceedings of the 3-rd Austrian Symposium on Geotechniques*, 167–180, Vienna, Austria, 2001.
11. P. FREIESLEBEN HANSEN and E.J. PEDERSEN, *Measurement device for controlling hardening of concrete* [in Norwegian] *Nordisk Betong*, **1**, 21–25, 1977.
12. KELLER GRUNDBAU GmbH, *The soilcrete – jet grouting process*, brochure 67–3E.
13. A.E. GROEN and R. DE BORST, *Three-dimensional finite element analysis of tunnels and foundations*, *HERON*, **42**, 4, 183–214, 1997.
14. CH. HELLMICH, M. LECHNER, R. LACKNER, J. MACHT, and H.A. MANG, *Creep in shotcrete tunnel shells*, [in:] S. MURAKAMI and N. OHNO, [Eds.], *Creep in Structures 2000 – Proceedings of the 5-th IUTAM Symposium on Creep in Structures*, 217–229, Nagoya Japan, 2001. Kluwer Academic Publishers, Dordrecht.
15. CH. HELLMICH, F.-J. ULM, and H. A. MANG, *Consistent linearization in finite element analysis of coupled chemo-thermal problems with exo- or endothermic reactions*, *Computational Mechanics*, **24**, 4, 238–244, 1999.
16. CH. HELLMICH, F.-J. ULM, and H. A. MANG, *Multisurface chemoplasticity I: Material model for shotcrete*, *Journal of Engineering Mechanics* (ASCE), **125**, 6, 692–701, 1999.

17. CH. HELLMICH, F.-J. ULM, and H. A. MANG, *Multisurface chemoplasticity II: Numerical studies on NATM-tunneling*, Journal of Engineering Mechanics (ASCE), **125**, 6, 702–714, 1999.
18. G. T. HOULSBY, *The use of a variable shear modulus in elastic-plastic models for clays*, Computers and Geotechnics, **1**, 3–13, 1985.
19. R. LACKNER, CH. HELLMICH, and H.A. MANG, *Constitutive modeling of cementitious materials in the framework of chemoplasticity*, International Journal for Numerical Methods in Engineering, **53**, 10, 2357–2388, 2002.
20. T. MARCHER and P.A. VERMEER, *Macromodelling of softening in non-cohesive soils*, [in:] P.A. VERMEER, S. DIEBELS, W. EHLERS, H.J. HERRMANN, S. LUDING, and E. RAMM [Eds.], *Continuous and discontinuous modelling of cohesive-frictional materials*, Lecture Notes in Physics, **568**, 89–108, Springer, Berlin 2001.
21. CH. PICHLER, R. LACKNER, L. MARTAK, and H.A. MANG, *Optimization of jet-grouted support in NATM tunneling*, International Journal for Numerical and Analytical Methods in Geomechanics, **28**, 7–8, 781–796, 2004.
22. CH. PICHLER, R. LACKNER, Y. SPIRA, and H.A. MANG, *Thermochemomechanical assessment of ground improvement by jet grouting in tunneling*, Journal of Engineering Mechanics (ASCE), **129**, 8, 951–962, 2003.
23. R.A. REGUEIRO and R.I. BORJA, *A finite element model of localized deformation in frictional materials taking a strong discontinuity approach*, Finite Elements in Analysis and Design, **33**, 4, 283–315, 1999.
24. W. RUETZ, *Creep of cement in concrete and the influence of simultaneous shrinkage on this type of creep* (in German), Deutscher Ausschluß für Stahlbeton, Heft 183, 1966.
25. A. SCHOFIELD and P. WROTH, *Critical state soil mechanics*, McGraw-Hill, London 1968.
26. J. SERCOMBE, CH. HELLMICH, F.-J. ULM, and H. A. MANG, *Modeling of early-age creep of shotcrete. I: model and model parameters*, Journal of Engineering Mechanics (ASCE), **126**, 3, 284–291, 2000.
27. J.C. SIMO and T.J.R. HUGHES, *Computational inelasticity*, Springer, Berlin 1998.
28. J.C. SIMO, J.G. KENNEDY, and S. GOVINDJEE, *Non-smooth multisurface plasticity and viscoplasticity. Loading/unloading conditions and numerical algorithms*, International Journal for Numerical Methods in Engineering, **26**, 2161–2185, 1988.
29. D. STERPI, *An analysis of geotechnical problems involving strain softening effects*, International Journal for Numerical and Analytical Methods in Geomechanics, **23**, 1427–1454, 1999.
30. F.-J. ULM, *Thermochemomechanical couplings in concretes: a first review* (in French), Technical report, Laboratoires des Ponts et Chaussées, Paris 1998.
31. F.-J. ULM and O. COUSSY, *Modeling of thermochemomechanical couplings of concrete at early ages*, Journal of Engineering Mechanics (ASCE), **121**, 7, 785–794, 1995.
32. F.-J. ULM and O. COUSSY, *Strength growth as chemo-plastic hardening in early age concrete*, Journal of Engineering Mechanics (ASCE), **122**, 12, 1123–1132, 1996.
33. F.J. ULM and O. COUSSY, *What is a “massive” concrete structure at early ages? Some dimensional arguments*, Journal of Engineering Mechanics, **127**, 5, 512–522, 2001.

34. I. VARDOLAKIS, M. GOLDSCHIEDER, and G. GUDEHUS, *Formation of shear bands in sand bodies as a bifurcation problem*, International Journal for Numerical and Analytical Methods in Geomechanics, **2**, 99–128, 1978.
35. P.A. VERMEER and R. DE BORST, *Non-associated plasticity for soils, concrete and rock*, HERON, **29**, 3, 3–64, 1984.
36. F.H. WITTMANN, *Creep and shrinkage mechanisms*, Chapter 6, 129–161, Wiley, Chichester 1982.
37. D.M. WOOD, *Soil Behaviour and critical state soil mechanics*, Cambridge University Press, Cambridge 1990.

*Received January 9, 2005, revised version May 11, 2005.*

---